Received 5 October 2019; revised 7 November 2019 and 15 November 2019; accepted 16 November 2019. Date of publication 28 November 2019; date of current version 3 January 2020. The review of this article was arranged by Editor K. Shenai.

Digital Object Identifier 10.1109/JEDS.2019.2956497

$Al_{0.75}Ga_{0.25}N/Al_xGa_{1-x}N/Al_{0.75}Ga_{0.25}N/AlN/SiC$ Metal–Oxide–Semiconductor Heterostructure Field-Effect Transistors With Symmetrically-Graded Widegap Channel

CHING-SUNG LEE [1], YAN-TING SHEN [1], WEI-CHOU HSU [2], YI-PING HUANG [2], AND CHENG-YANG YOU [2]

1 Department of Electronic Engineering, Feng Chia University, Taichung 40857, Taiwan
2 Institute of Microelectronics, Department of Electrical Engineering, National Cheng Kung University, Tainan 70101, Taiwan

CORRESPONDING AUTHOR: C.-S. LEE (e-mail: cslee@fcu.edu.tw)

This work was supported by the Ministry of Science and Technology, Taiwan, under Contract MOST 108-2221-E-035-038-MY3.

ABSTRACT Novel $Al_{0.75}Ga_{0.25}N/Al_xGa_{1-x}N/Al_{0.75}Ga_{0.25}N/AlN$ metal-oxide-semiconductor heterostructure field-effect transistors (MOS-HFETs) with symmetrically-graded widegap $Al_xGa_{1-x}N$ channel ($x = 0.75 \rightarrow 0.25 \rightarrow 0.75$) grown on a SiC substrate are investigated. Al_2O_3 was devised as the gate dielectric by using a non-vacuum ultrasonic spray pyrolysis deposition (USPD) technique. Device characteristics with respect to different etch depths of the source/drain recesses were studied. For a 2-μm gate length (L_G), the present widegap V-shape-channel MOS-HFET has shown improved maximum drain-source current density ($I_{DS,max}$) of 299.3 A/mm at $V_{DS} = 20$ V, I_{DS} density at $V_{GS} = 0$ V (I_{DSS0}) of 153.9 mA/mm, on/off-current ratio (I_{on}/I_{off}) of 1.4×10^7, extrinsic transconductance ($g_{m,max}$) of 16.7 mS/mm, two-terminal off-state gate-drain breakdown voltage (BV_{GD}) of -379 V, and three-terminal on-state drain-source breakdown voltage (BV_{DS}) of 339 V. Besides, superior deep-UV sensing performance with high spectral responsivity (SR) of 1780 (810.2) A/W at wavelength $\lambda = 250$ (300) nm are also achieved.

INDEX TERMS $Al_xGa_{1-x}N$, MOS-HFET, symmetrically-graded, widegap channel, Al_2O_3, non-vacuum ultrasonic spray pyrolysis deposition, spectral responsivity, deep-UV.

I. INTRODUCTION

Gan-based heterostructure field-effect transistors (HFETs) have been widely used due to their advantages of high speed, high power efficiency, and low switching loss [1]–[2]. Various device design approaches have been studied to increase drain current density, reduce gate leakage, and extend breakdown voltage, including uses of metal-oxide-gate (MOS-gate) [3]–[5], field-plate (FP) [6]–[8], Schottky-source/drain [9], and trench [10] structures. Different epitaxial structures have also been investigated, such as strain-induced polarization AlGaN/GaN heterostructure [11], and lattice-matched, high polarization, and large conduction-band discontinuity (ΔE_C) InAlN/GaN heterostructure [12]–[13], AlN substrate [14]–[15]. In order to meet the requirement of high-voltage power-switching applications, devices with widegap AlGaN channel have lately been studied [16]–[18]. The bandgap of AlN is 6.2 eV which is almost two times of GaN, while exhibiting comparable saturation velocity of 2.2×10^7 cm^2/V-s. The critical electric field for breakdown in AlGaN can be devised from 3.3 MV/cm in GaN to 12 MV/cm in AlN. Higher Johnson's figure-of-merit (JFOM) [19] and Baliga's figure-of-merit (JFOM) [20] of AlGaN channel indicate the promising applications for high-voltage power switching

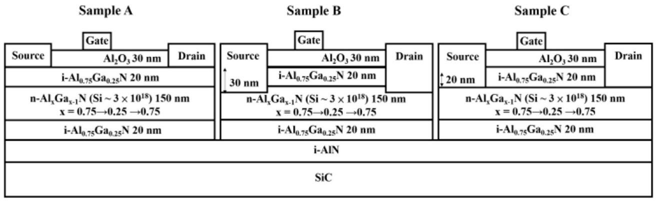

FIGURE 1. (a) Schematic device diagram of the present Al_2O_3-dielectric $Al_{0.75}Ga_{0.25}N/Al_xGa_{1-x}N/Al_{0.75}Ga_{0.25}N$/AlN MOS-HFETs with different source/drain etching depths of (a) 0 nm (sample A), (b) 30 nm (sample B), and (c) 20 nm (sample C), respectively.

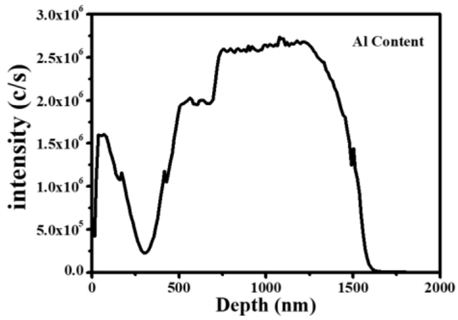

FIGURE 2. The SIMS profile of Al content for the epitaxial sample.

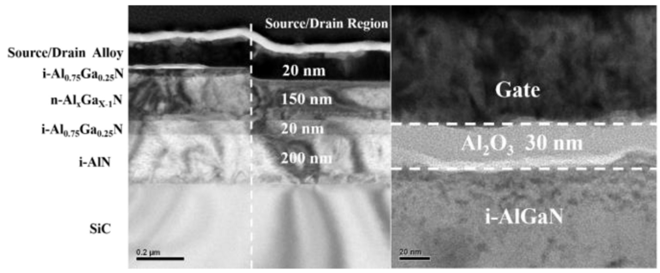

FIGURE 3. The TEM photos showing the cross-sectional source/drain recess region (left) and the MOS-gate structure (right) for sample C.

device designs. Besides, the direct bandgap property of widegap AlGaN can also provide deep-UV sensing [11]–[21] capability. This work presents novel Al_2O_3-dielectric $Al_{0.75}Ga_{0.25}N/Al_xGa_{1-x}N/Al_{0.75}Ga_{0.25}N$/AlN MOS-HFET design with symmetrically-graded widegap $Al_xGa_{1-x}N$ channel ($x = 0.75 \rightarrow 0.25 \rightarrow 0.75$) grown on a SiC substrate. The gate oxide was grown by using a cost-effective non-vacuum ultrasonic spray pyrolysis deposition (USPD) [22] technique. As compared to other deposition techniques, the USPD has advantages of high deposition rate, room-temperature operation, and non-vacuum environment. Improved device characteristics with respect to different etching depths of source/drain recesses are investigated. High spectral responsivity (SR) and bias-dependent deep-UV sensing capability are also achieved for the present MOS-HFET design.

II. MATERIAL GROWTH AND DEVICE FABRICATION

Figs. 1(a)-(c) show the schematic device diagram of the studied Al_2O_3-dielectric $Al_{0.75}Ga_{0.25}N/Al_xGa_{1-x}N/Al_{0.75}Ga_{0.25}N$/ AlN MOS-HFETs with different etching depths of 0 nm (sample A), 30 nm (sample B), and 20 nm (sample C) for the source/drain recesses, respectively. All three samples have the same layer structure grown by using a low-pressure metal-organic chemical vapor deposition (LP-MOCVD) system. Upon a SiC substrate, the epitaxial structure consists of an intrinsic AlN buffer layer, a 20-nm intrinsic $Al_{0.75}Ga_{0.25}N$ barrier, a 150-nm n-type $Al_xGa_{1-x}N$ channel (Si $\sim 3 \times 10^{18}$ cm^{-3}), and a 20-nm intrinsic $Al_{0.75}Ga_{0.25}N$ barrier. The Al composition of the $Al_xGa_{1-x}N$ channel was varied linearly to be $x = 0.75 \rightarrow 0.25 \rightarrow 0.75$. Channel doping was introduced to further increase the conductivity and current densities. The secondary ion-mass spectroscopy (SIMS) profile of Al content for the epitaxial sample, as shown in Fig. 2, has verified the devised symmetrically-graded AlGaN V-shape widegap channel.

Standard photolithography and lift-off techniques were used for device fabrication [23]. All three samples were fabricated at the same time. Mesa etching was first conducted by using an inductively coupled-plasma reactive ion etcher (ICP-RIE). The etching barrier is 100-nm thick Ni layer. The mixed etching gases are BCl_3 and Cl_2 with flow rates of 10 sccm and 20 sccm, respectively. The power settings for ICP/RIE are 75/120 W. After the source/drain photolithography, different etching depths of 0 nm, 30 nm, and 20 nm were formed respectively for samples A-C before metallization. The dry etching rate is about 25 nm/min. Then, metal stacks of Ti (10 nm)/Al (50 nm)/Ni (10 nm)/Au (50 nm) were evaporated as the source/drain electrodes. The samples were annealed under 900°C for 30 seconds to form ohmic contact by using a ULVAC MILA-5000 rapid thermal annealing (RTA) system. Before gate deposition, a 30-nm thick Al_2O_3 layer was deposited on the $Al_{0.75}Ga_{0.25}N$ barrier surface between the drain/source electrodes as the gate dielectric. Finally, Ni (100 nm)/Au (50 nm) metal stacks were evaporated as the gate electrode to complete the device fabrication. The gate dimensions are $2 \times 100\ \mu m^2$ with gate-to-drain/source spacings of 6/2 μm for samples A-C. The studied devices were fabricated at the same time on separate samples. A control MOS-HFET device with same epitaxial structure, except for with an intrinsic $Al_{0.5}Ga_{0.5}N$ channel was fabricated in comparison. The Al composition was set to be 0.5, which is equivalent to the Al content of the symmetrically-graded $Al_xGa_{1-x}N$ ($x = 0.75 \rightarrow 0.25 \rightarrow 0.75$) channel in the present sample C.

III. EXPERIMENTAL RESULTS AND DISCUSSION

Fig. 4 shows the common-source current-voltage ($I_{DS} - V_{DS}$) characteristics of samples A-C at 300 K, measured by using a KEITHLEY 4200 analyzer. The V_{GS} voltage was varied from 10 V to −25 V at −5 V/step. Good pinch-off was observed in the studied devices. The transfer extrinsic transconductance (g_m) and saturated drain-source current (I_{DS}) density as functions of V_{GS} for samples A-C biased at V_{DS} = 20 V are shown in Fig. 5. The maximum

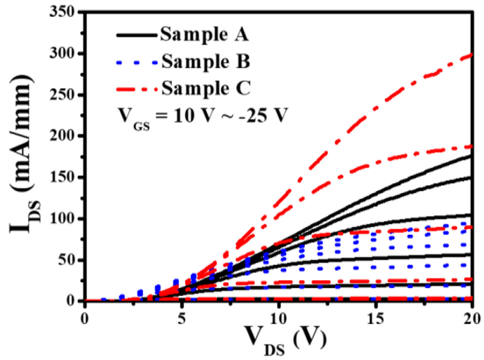

FIGURE 4. Common-source $I_{DS} - V_{DS}$ characteristics of samples A-C at 300 K.

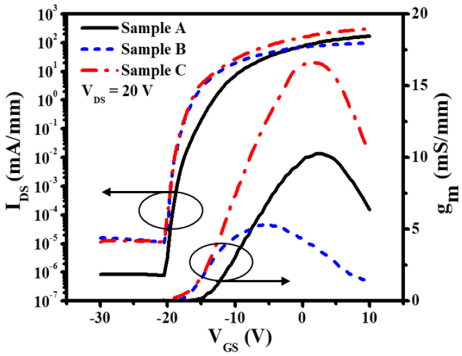

FIGURE 5. Transfer g_m and I_{DS} as functions of V_{GS} for samples A-C at 300 K.

I_{DS} ($I_{DS,\ max}$) density at $V_{DS} = 20$ V and I_{DS} at $V_{GS} = 0$ V (I_{DSS0}) were characterized to be 181.3 mA/mm and 75.8 mA/mm for sample A, 102.1 mA/mm and 68.8 mA/mm for sample B, and 299.3 mA/mm and 153.9 mA/mm for sample C. The corresponding on/off-current ratios (I_{on}/I_{off}) were determined to be 4.5×10^8, 1.3×10^7, and 1.4×10^7. Comparable I_{on}/I_{off} characteristics were obtained in all three devices, since the gate insulation and surface passivation effect have been enhanced by the similar MOS-gate design. Nevertheless, sample C has exhibited the highest maximum g_m ($g_{m,\ max}$) of 16.7 mS/mm, as compared to 10.2 mS/mm in sample A and 6.0 mS/mm in sample B. It can be seen that the device characteristics are strongly influenced by the different source/drain recess structures. Besides, the obtained I_{DS} densities and device gain of samples A-C are all superior to $I_{DS,\ max}$ (I_{DSS0}) of 83.8 (53.3) mA/mm and $g_{m,\ max}$ of 3.7 mS/mm of the control sample. Fig. 6 shows the $I_{DS,\ max}$ characteristics as functions of V_{DS} for sample C biased at $V_{GS} = 10$ V at ambient temperatures of 300 K, 350 K, and 400 K, respectively. The I_{DS} densities were observed with the ambient temperature. The corresponding $I_{DS,\ max}$ are 299.3 mA/mm, 312.7 mA/mm, and 343.6 mA/mm. It is mainly due to the increased 2DEG concentration due to enhanced thermal ionization of the devised channel doping.

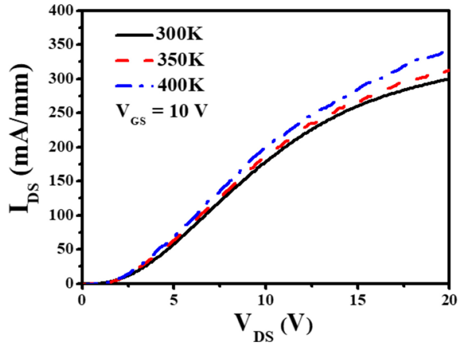

FIGURE 6. $I_{DS,max}$ characteristics as functions of V_{DS} for sample C biased at $V_{GS} = 10$ V at 300 K, 350 K, and 400 K.

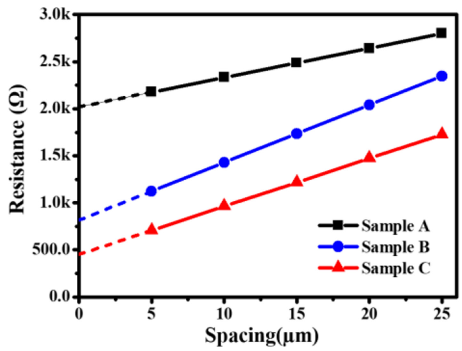

FIGURE 7. The measured TLM characteristics for samples A-C at 300 K.

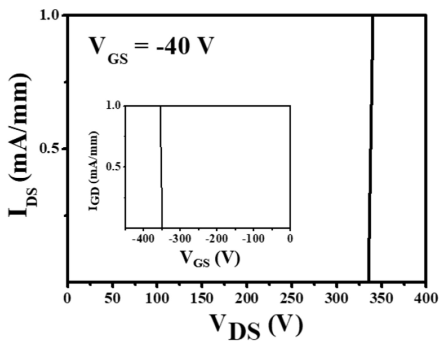

FIGURE 8. BV_{DS} characteristics at 300 K of sample C biased at $V_{GS} = -40$ V. The inset shows the BV_{GD} characteristics.

The dynamic turn-on resistance (R_{on}) was also characterized from Fig. 4. Sample C has the lowest R_{on} of 63 Ω-mm, as compared to 112 Ω-mm in sample A and 164 Ω-mm in sample B. It is mainly due to the source/drain ohmic contact properties with respect to the different recess depths. The transfer length measurement [24] test structures were applied to characterize the contact resistances (R_c) for the studied devices. Fig. 7 shows the measured resistances at different transfer lengths of 5 μm, 10 μm, 15 μm, 20 μm, and 25 μm for samples A-C at 300 K. The specific contact resistivity (ρ_c) values for samples A-C were calculated to be 3.3×10^{-2} Ω-cm^2, 2.7×10^{-3} Ω-cm^2, and 9.9×10^{-4} Ω-cm^2, with the approximated R_c of 1.0×10^3 Ω-mm, 4.1×10^2 Ω-mm, and 2.3×10^2 Ω-mm. Therefore,

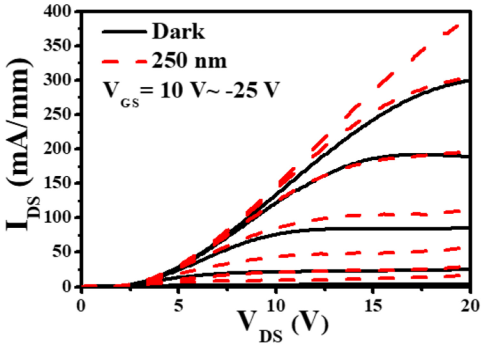

(a)

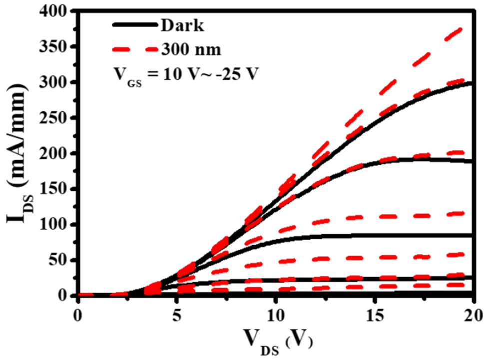

(b)

FIGURE 9. **Common-source $I_{DS} - V_{DS}$ characteristics of sample C in the dark and under deep-UV illuminations of (a) λ = 250 nm and (b) λ = 300 nm.**

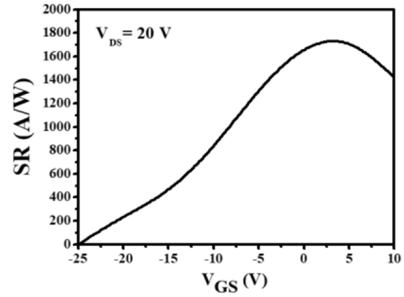

(a)

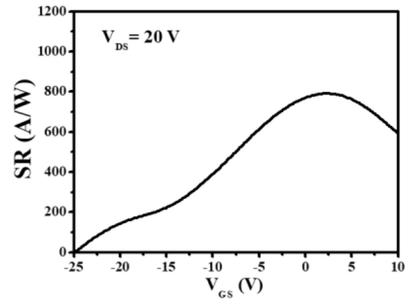

(b)

FIGURE 10. **Bias-dependent SR charactreristics of sample C under deep-UV illuminations of (a) λ = 250 nm and (b) λ = 300 nm.**

sample C with the recess depth of 20 nm has demonstrated the best source/drain ohmic contact property and optimum device performance. Hall measurement was performed under a magnetic field of 5000 G at 300 K. Sample C and the control sample have the comparable two-dimensional electron gas concentration (n_{2DEG}) of 1.69 × 10^{10} cm^{-2} and 1.64 × 10^{10} cm^{-2}. Yet, much higher electron mobility (μ_n) of 168 cm^2/V-s was obtained in sample C than 13 cm^2/V-s in the control sample. It is mainly due to the design of symmetrically-graded $Al_xGa_{1-x}N$ channel. The 2DEG was mainly confined at the bottom of the V-shape channel. The carrier transport was improved within the low Al-composition region. Higher $\mu_n - n_{2DEG}$ product of 2.84 × 10^{12} $V^{-1}-s^{-1}$ has been obtained in sample C than 2.1 × 10^{11} $V^{-1}-s^{-1}$ in the control sample. Enhanced channel conductivity and current density are expected by the symmetrically-graded $Al_xGa_{1-x}N$ channel design. The optimum $I_{DS,max}$, I_{DSS0}, and $g_{m,max}$ performances at 300 K of the present MOS-HFET with V-shaped $Al_xGa_{1-x}N$ widegap channel are 299.3 mA/mm, 153.9 mA/mm, and 16.7 mS/mm, which are also superior to 83.7 mA/mm, 53.3 mA/mm, and 3.7 mS/mm of the control MOS-HFET device under the same device fabrication process. The present sample C are also superior to other works of $g_{m,max}$ = 15 mS/mm at $L_G = 1\mu m$ [25], $I_{DS,max}$ = 114 mA/mm at $L_G = 1\mu m$ [26], and $g_{m,max}$ = 2.4 mS/mm and $I_{DS,max}$ = 13 mA/mm at $L_G = 9\mu m$ [27].

Fig. 8 shows three-terminal on-state drain-source breakdown voltage (BV_{DS}) characteristics at 300 K for sample C biased at V_{GS} = −40 V. The inset shows its two-terminal off-state gate-drain breakdown voltage (BV_{GD}) characteristics at 300 K. BV_{DS} and BV_{GD} were determined as the corresponding I_{DS} and I_{GD} densities are equal to 1 mA/mm. Sample C has demonstrated superior BV_{DS} of 339 V and BV_{GD} of −379 V, as compared to 275 V and −375 V in other work [25]. The enhanced BV_{DS} and BV_{GD} performances are contributed by the MOS-gate and V-shape $Al_xGa_{1-x}N$ channel designs. In addition to surface passivation by using USPD and enhanced gate insulation due to the widegap gate-oxide of Al_2O_3, the gate leakage was further suppressed by the increased energy barrier for thermionic emission of the 2DEG in the V-shape channel. Besides, as the 2DEG was pushed towards the buffer by the decreased V_{GS}, the critic electric field for effective impact ionization was increased since the Al-ratio near buffer was higher than that at the center of the V-shape channel. Consequently, enhanced BV_{DS} and BV_{GD} are achieved.

Besides, wide and direct bandgap properties of AlGaN are suitable for deep-UV detection applications. High absorption efficient can be obtained, since it is insensitive to visible and infrared radiation. Figs. 9(a)-9(b) compare the typical $I_{DS} - V_{DS}$ curves of sample C in the dark and under deep-UV illumination at wavelengths of 250 nm and

300 nm, respectively. The related bias-dependent SR performances of sample C biased at $V_{DS} = 20$ V was also illustrated in Figs. 10(a)-10(b). Maximum SR was observed at $V_{GS} = 2.5$ V for both UV radiations. The V_{GS} bias for peak SR in sample C is identical to that for obtaining $g_{m,max}$, as shown in Fig. 5. The increased I_{DS} densities under UV illumination were believed to be contributed by the device gain due to photovoltaic effect. The photo-generated excess carriers were stimulated by decreased potential barrier in the AlGaN channel. Similar phenomena were observed in other works [29]–[30]. The optical power for 250 (300)-nm deep-UV light source is 6.5 (14.7) μW. The I_{DS} densities for sample C biased at $V_{GS} = 2.5$ V and $V_{DS} = 20$ V were 173.4 (173.4) mA/mm and 289.4 (292.8) mA/mm in the dark and under the UV radiation of $\lambda = 250$ (300) nm. The corresponding optical I_{DS} densities were calculated to be 115.7 (119.1) mA/mm. Superior SR performances of 1780 A/W and 810.2 A/W have been achieved for the deep-UV radiation wavelengths of 250 nm and 300 nm, respectively. The present UV sensing performance is superior to 360 A/W at $\lambda = 350$ nm of InAlN/AlN/GaN MOS-HFET [28], 34 A/W at $\lambda = 367$ nm of InAlN/GaN stack photodiode (PD) [31], and other PDs [32]–[33]. Excellent SR was contributed by the device gain and noise immunity of the widegap AlGaN channel of the present design.

IV. CONCLUSION

Novel Al_2O_3-dielectric $Al_{0.75}Ga_{0.25}N/Al_xGa_{1-x}N/Al_{0.75}Ga_{0.25}N$ /AlN MOS-HFETs with symmetrically-graded widegap $Al_xGa_{1-x}N$ channel (x = 0.75 → 0.25 → 0.75) grown on a SiC substrate have been successfully investigated. Optimum source/drain ohmic contacts and device performance have been obtained as the source/drain recess depths are equal to 20 nm. Enhanced current drive and breakdown characteristics have also been obtained by the devised symmetrically-graded widegap $Al_xGa_{1-x}N$ channel and MOS-gate structures. Superior $I_{DS,max}$ of 299.3 A/mm, I_{DSS0} of 153.9 mA/mm, I_{on}/I_{off} of 1.4×10^7, $g_{m,max}$ of 16.7 mS/mm, BV_{GD} of −379 V, and BV_{DS} of 339 V have been achieved. Excellent deep-UV SR performance of 1780 (810.2) A/W for $\lambda = 250$ (300) nm have also been achieved. The present MOS-HFET design with symmetrically-graded widegap $Al_xGa_{1-x}N$ channel is promising for high-voltage circuits and deep-UV active sensing applications.

REFERENCES

[1] L. Shen *et al.*, "AlGaN/AlN/GaN high-power microwave HEMT," *IEEE Electron Device Lett.*, vol. 22, no. 10, pp. 457–459, Oct. 2001.

[2] C. Y. Tsai, T. L. Wu, and A. Chin, "High-performance GaN MOSFET with high-κ $LaAlO_3/SiO_2$ gate dielectric," *IEEE Electron Device Lett.*, vol. 33, no. 1, pp. 35–37, Jan. 2012.

[3] C.-S. Lee, W.-C. Hsu, B.-J. Chiang, H.-Y. Liu, and H.-Y. Lee, "Comparative studies on AlGaN/GaN/Si MOSHFETs with Al2O3/TiO2 stacked dielectrics by using an ultrasonic spray pyrolysis deposition technique," *Semicond. Sci. Technol.*, vol. 32, no. 5, pp. 1–7, Apr. 2017.

[4] C.-S. Lee, W.-C. Hsu, H.-Y. Liu, and B.-J. Chiang, "Ti0.5Al0.5Odielectric AlGaN/GaN/Si metal-oxide-semiconductor heterostructure field-effect transistors by using non-vacuum ultrasonic spray pyrolysis deposition," *ECS J. Solid-State Sci. Technol.*, vol. 5, no. 12, pp. Q284–Q288, Dec. 2016.

[5] T. Huang, X. Zhu, K. M. Wong, and K. M. Lau, "Low-leakagecurrent AlN/GaN MOSHFETs using Al_2O_3 for increased 2DEG," *IEEE Electron Device Lett.*, vol. 33, no. 2, pp. 212–214, Feb. 2012.

[6] Y. Dora, A. Chakraborty, L. mccarthy, S. Keller, S. P. denbaars, and U. K. Mishra, "High breakdown voltage achieved on AlGaN/GaN HEMTs with integrated slant field plates," *IEEE Electron Device Lett.*, vol. 27, no. 9, pp. 713–715, Sep. 2006.

[7] S. Karmalkar and U. K. Mishra, "Enhancement of breakdown voltage in AlGaN/GaN high electron mobility transistors using a field plate," *IEEE Trans. Electron Devices*, vol. 48, no. 8, pp. 1515–1521, Aug. 2001.

[8] C. S. Lee *et al.*, "Investigations of novel *Gamma*-gate MOSHEMTs by ozone water oxidation and shifted exposure techniques," *IEEE Trans. Electron Device*, vol. 58, no. 9, pp. 2981–2989, Sep. 2011.

[9] Q. Zhou *et al.*, "Schottky-contact technology in InAlN/GaN HEMTs for breakdown voltage improvement," *IEEE Trans. Electron Devices*, vol. 60, no. 3, pp. 1075–1081, Mar. 2013.

[10] W. Li *et al.*, "Development of GaN vertical trench-MOSFET with MBE regrown channel," *IEEE Trans. Electron Devices*, vol. 65, no. 6, pp. 2558–2564, Jun. 2018.

[11] M. A. Khan, M. S. Shur, Q. Chen, J. N. Kuznia, and C. J. Sun, "Gated photodetector based on GaN/AlGaN heterostructure field effect transistor," *Electron. Lett.*, vol. 31, no. 5, pp. 398–400, Mar. 1995.

[12] D. S. Lee, X. Gao, S. Guo, and T. Palacios, "InAlN/GaN HEMTs with AlGaN back barriers," *IEEE Electron Device Lett.*, vol. 32, no. 5, pp. 617–619, May 2011.

[13] C.-S. Lee, W.-C. Hsu, H.-Y. Liu, and Y.-C. Chen, "Al_2O_3-dielectric $In_{0.18}Al_{0.82}N$/AlN/GaN/Si metal–oxide–semiconductor heterostructure field-effect transistors with backside substrate metal-trench structure," *IEEE J. Electron Devices Soc.*, vol. 6, no. 1, pp. 68–73, Dec. 2017.

[14] A. Saxler, P. Kung, C. J. Sun, E. Bigan, and M. Razeghi, "High quality aluminum nitride epitaxial layers grown on sapphire substrates," *Appl. Phys. Lett.*, vol. 64, no. 3, pp. 339–341, 1994.

[15] Y. Kumagai *et al.*, "Preparation of a freestanding AlN substrate from a thick AlN layer grown by hydride vapor phase epitaxy on a bulk AlN substrate prepared by physical vapor transport," *Appl. Phys. Exp.*, vol. 5, no. 5, 2012, Art. no. 055504.

[16] T. Nanjo *et al.*, "AlGaN channel HEMT with extremely high breakdown voltage," *IEEE Trans. Electron Devices*, vol. 60, no. 3, pp. 1046–1053, Mar. 2013.

[17] T. Nanjo *et al.*, "First operation of AlGaN channel high electron mobility transistors," *Appl. Phys. Exp.*, vol. 1, no. 1, pp. 1–3, Jan. 2008.

[18] M. Xiao *et al.*, "High performance $Al_{0.10}Ga_{0.90}N$ channel HEMTs," *IEEE Electron Device Lett.*, vol. 39, no. 8, pp. 1149–1151, Aug. 2018.

[19] E. Johnson, "Physical limitations on frequency and power parameters of transistors," *RCA Rev.*, vol. 26, pp. 163–177, Jun. 1965.

[20] B. J. Baliga, "Semiconductors for high-voltage, vertical channel field-effect transistors," *J. Appl. Phys.*, vol. 53, no. 3, pp. 1759–1764, Mar. 1982.

[21] M. Martens *et al.*, "High gain ultraviolet photodetectors based on AlGaN/GaN heterostructures for optical switching," *Appl. Phys. Lett.*, vol. 98, no. 21, May 2011, Art. no. 211114.

[22] B.-Y Chou *et al.*, "Al_2O_3-passivated AlGaN/GaN HEMTs by using nonvacuum ultrasonic spray pyrolysis deposition technique," *IEEE Electron Device Lett.*, vol. 35, no. 9, pp. 903–905, Sep. 2014.

[23] Y. T. Shen, "Investigations on Al_xGa1_xN/AlN/SiC heterostructure field-effect transistors with V-shaped wide-gap channel design," M.S. thesis, Dept. Electron. Eng., Feng Chia Univ., Taichung, Taiwan, Jun. 2019.

[24] D. K. Schroder, *Semiconductor Materials and Device Characterization*. New Jersey, USA: Wiley, 2003.

[25] S. Bajaj *et al.*, "High Al-content AlGaN transistor with 0.5 A/mm current density and lateral breakdown field exceeding 3.6 MV/cm," *IEEE Electron Device Lett.*, vol. 39, No. 2, pp. 256–259, Feb. 2018

[26] T. Nanjo *et al.*, "Remarkable breakdown voltage enhancement in AlGaN channel high electron mobility transistors," *Appl. Phys. Lett.*, vol. 92, no. 26, Jun. 2008, Art. no. 263502.

[27] H. Tokuda *et al.*, "High Al composition AlGaN-channel high-electron-mobility transistor on AlN substrate," *Appl. Phys. Exp.*, vol. 3, Dec. 2010, Art. no. 121003.

[28] C.-S. Lee, X.-C. Yao, Y.-P. Huang, and W.-C. Hsu, "Improved ultraviolet detection and device performance of Al_2O_3-dielectric $in_{0.17}Al_{0.83}N$/AlN/GaN MOS-HFETs," *IEEE J. Electron Devices Soc.*, vol. 7, no. 1, pp. 430–434, Mar. 2019.

[29] A. Caddemi, E. Cardillo, S. Patanè, and C. Triolo, "An accurate experimental investigation of an optical sensing microwave amplifier," *IEEE Sensors J.*, vol. 18, no. 22, pp. 9214–9221, Nov. 2018.

[30] Y. Takanashi, K. Takahata, and Y. Muramoto, "characteristics of InAlAs/InGaAs high-electron mobility transistors under illumination with modulated light," *IEEE Trans. Electron Devices*, vol. 46, no. 12, pp. 2271–2277, Dec. 1999.

[31] S. Kumar, A. S. Pratiyush, S. B. Dolmanan, S. Tripathy, R. Muralidharan, and D. N. Nath, "UV detector based on InAlN/GaN-on-Si HEMT stack with photo-to-dark current ratio $> 10^7$," *Appl. Phys. Lett.*, vol. 111, no. 25, Dec. 2017, Art. no. 251103.

[32] S. Chang, M. Chang, and Y. Yang, "Enhanced responsivity of GaN metal–semiconductor–metal (MSM) photodetectors on GaN substrate," *IEEE Photon. J.*, vol. 9, no. 2, Apr. 2017, Art. no. 6801707.

[33] D. Li *et al.*, "Realization of a high-performance GaN UV detector by nanoplasmonic enhancement," *Adv. Mater.*, vol. 24, pp. 845–849, Feb. 2012.